Validation of a Numerical Quasi-One-Dimensional Model for Wave Rotor Turbines With Curved Channels

Stefan Tüchler[1]
Powertrain and Vehicle Research Centre,
Department of Mechanical Engineering,
University of Bath,
Bath BA2 7AY, UK
e-mail: S.Tuechler@bath.ac.uk

Colin D. Copeland
Powertrain and Vehicle Research Centre,
Department of Mechanical Engineering,
University of Bath,
Bath BA2 7AY, UK

A wave rotor is a shock-driven pressure exchange device that, while relatively rarely studied or indeed, employed, offers significant potential efficiency gains in a variety of applications including refrigeration and gas turbine topping cycles. This paper introduces a quasi-one-dimensional (Q1D) wave action model implemented in MATLAB *for the computation of the unsteady flow field and performance characteristics of wave rotors of straight or cambered channel profiles. The purpose here is to introduce and validate a rapid but reliable method of modeling the performance of a power-generating wave rotor where little such insight exists in open literature. The model numerically solves the laminar one-dimensional (1D) Navier–Stokes equations using a two-step Richtmyer time variation diminishing (TVD) scheme with minmod flux limiter. Additional source terms account for viscous losses, wall heat transfer, flow leakage between rotor and stator endplates as well as torque generation through momentum change. Model validation was conducted in two steps. First of all, unsteady and steady predictive capabilities were tested on three-port pressure divider rotors from open literature. The results show that both steady port flow conditions as well as the wave action within the rotor can be predicted with good agreement. Further validation was done on an in-house developed and experimentally tested four-port, three-cycle, throughflow microwave rotor turbine featuring symmetrically cambered passage walls aimed at delivering approximately 500 W of shaft power. The numerical results depict trends for pressure ratio, shaft power, and outlet temperature reasonably well. However, the results also highlight the need to accurately measure leakage gaps when the machine is running in thermal equilibrium.*
[DOI: 10.1115/1.4044286]

Introduction

Over the past decades, numerous research studies have been dedicated toward the investigation of dynamic pressure exchange machinery, such as wave rotors. These devices use the energy carried in moving shock waves to transfer energy from one stream of fluid to another without the need to incorporate additional mechanical parts. This advantage, in combination with relatively large pressure ratio gains through shock wave compression and a high efficiency associated with this process, renders wave action devices an attractive technology for power generation.

Opposed to crypto-steady flow devices, such as turbomachinery, wave rotors are inherently unsteady flow devices, where shock and expansion waves travel along discrete channels arranged around the circumference of a cylindrical drum. To each side of the spinning rotor, there are stator endplates containing port openings, as shown in Fig. 1. Exposing the rotor channels periodically to the ports then triggers shock and expansion waves.

The application range for wave rotors outlined by the literature is diverse. The bulk of early studies focused on pressure exchangers with straight passage profiles for gas turbine topping cycles [1–8] and supercharging devices for internal combustion engines [9–16]. In recent years, the application to refrigeration cycles [17–19] and pressure-gain combustors [20–22] has come into the focus of consideration.

In comparison, little amount of attention has been given to wave turbines with cambered passage walls aimed at acting both as pressure exchangers while producing shaft power through momentum change of the flow [23–27]. Documentation of these endeavors is unfortunately fragmentary. The best documented and most successful example of a wave rotor engine was done by Pearson [23,24] at the University of Bath. Initial tests were conducted on a single cycle, through-flow wave rotor with helical passage shape leading to a power output of around 26 kW at a rotational speed of 18,000 rpm. Further research was suspended after the engine was destroyed due to overspeeding. Further experiments by General Electric and General Power Corporation yielded insufficient shaft power generation and were not further pursued [25,26].

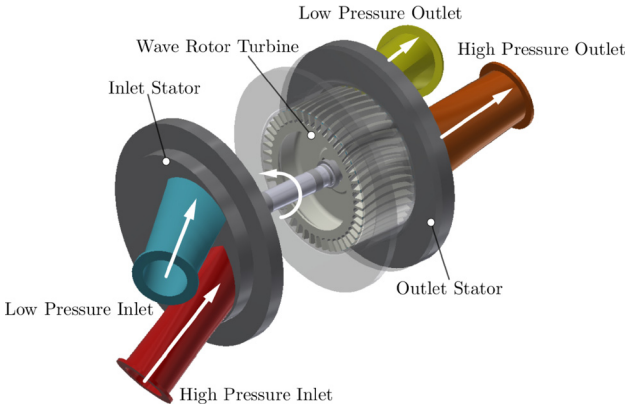

Fig. 1 Wave rotor structure showing wave rotor with discrete passages, in- and outlet stator as well as the arrangement of ports

[1]Corresponding author.

Manuscript received June 25, 2019; final manuscript received June 27, 2019; published online January 17, 2020. Editor: Jerzy T. Sawicki.

One limitation of early efforts on wave rotor design was partially due to a lack in computational power rendering performance estimation time consuming (in particular when done by hand calculations) and often inaccurate. To mitigate this and to accurately compute unsteady wave action in the rotor channels and steady conditions in the ports as well as wave rotor performance parameters, one-dimensional (1D) codes have established themselves as swift and reliable tools. This has been pursued by a number of institutions, ranging from the Naval Postgraduate School [28–32], University of Tokyo [6,33,34], ONERA [6,35,36], Michigan State University [37], NASA Glenn Research Center [38–42] as well as Xiamen University/Beihang University [43,44] most recently.

While most of the mentioned studies deal with straight channels, there is merely one study that incorporates passage curvature in a one-dimensional environment, albeit at reduced order through a passage-averaged description. This was conducted at NASA Glenn Research Center by Welch and Paxson [42] and compared port axial and tangential velocities as well as predicted power output to a two-dimensional computational fluid dynamics (CFD) simulation. However, no comparison with experimental data was done.

Against this background, this paper aims at addressing this gap by introducing a one-dimensional model that allows a reliable and cost effective insight into the performance of wave rotors with straight and arbitrarily shaped camber. To the authors' knowledge, this paper will present, for the first time, a quasi-one-dimensional (Q1D) model that allows direct computation of torque output for cambered wave rotor channels without the need for further model reduction. It is also the first time such a model has been compared to experiments. Conventional 1D models for turbines and compressors employ either a map-based approach that requires a priori experimental data in the form of mass flow rate, efficiency, and pressure ratio [45] or model the rotor wheel through an adiabatic pressure loss that is calibrated over the anticipated flow range against experimental data [46]. The proposed model, however, differs to that approach as directly models the unsteady wave action dynamics within the rotor while accounting for finite passage opening, friction, leakage, and inviscid forces.

The structure of the paper is thus as follows: first, the governing equations and model source terms for viscous and inviscid forces, flow leakage, and wall heat transfer are introduced; second, steady and unsteady validation of the code is done based on experimental data from the open literature on pressure dividers done by Kentfield [47] and NASA [48]. Further validation of the model is achieved through experimental data from a wave rotor turbine experiment performed in the gas stand at the University of Bath. The wave rotor turbine features a symmetrical, arc-shaped passage design that was designed to produce a power output of up to 500 W.

Simulation Model

The model was implemented in MATLAB R2017 and follows a single wave rotor passage of constant cross section as it passes ports along the circumference. It consists of numerical routines to solve the one-dimensional conservation equations accounting for channel curvature for shaft power extraction, heat transfer between fluid and rotor walls, flow leakage in the axial clearance between stator and rotor, as well as gradual passage opening effects. The code can be applied to both through-flow and reverse-flow wave rotor applications.

Finally, the user has the option of defining the gas composition for the operating medium. Throughout this study, this is assumed to be air, composed of 79% nitrogen and 21% oxygen.

For the derivation of the model, a number of assumptions are made; first of all, in order to justify a one-dimensional formulation, channel length is expected to be an order of magnitude larger than channel width and height. Furthermore, the flow path follows a single streamline through the passage. The quasi-one-dimensional formulation assumes that all quantities are uniform across the cross section. This does not hold for wave rotors, as high rotational speeds due to centrifugal effects, vortices due to finite passage opening effects, and shock-wave boundary layer interactions create secondary flows and skewed air/gas demarcation surfaces, which cannot be captured using one-dimensional wave action codes. While the effect of gradual passage opening on the primary shock strength can at least be qualitatively captured, interferences between neighboring channels and between the channel and leakage cavity, which become particularly pronounced for larger axial clearances between rotor and stator, cannot be depicted directly.

Governing Equations. The equations used to describe the unsteady, compressible, and viscous effects taking place within a wave rotor turbine are the one-dimensional Navier–Stokes equations, which can be written in conservative form as

$$\frac{\partial \mathbf{U}}{\partial t} + \frac{\partial \mathbf{F}(\mathbf{U})}{\partial m} = \mathbf{S} \tag{1}$$

The first term represents time-dependent variations, while the second term refers to advection. The source term **S** accounts for viscous as well as inviscid effects (i.e., friction and "blade" forces), as well as leakage losses and wall heat transfer. These will be explained in more detail in the section Source Terms. The state vector **U** and the flux vector **F** are defined as

$$\mathbf{U} = \begin{pmatrix} \rho \\ \rho u \\ \rho E \end{pmatrix}, \quad \mathbf{F} = \begin{pmatrix} \rho u \\ \rho u^2 + p - \tau_{mm} \\ \rho u\left(E + \dfrac{p}{\rho} - \tau_{mm} + q_m\right) \end{pmatrix} \tag{2}$$

Heat conduction within the fluid is addressed through Fourier's law of heat conduction. Furthermore, friction between particles is included through shear force. They can be more explicitly stated as

$$q_m = -k\frac{\partial T}{\partial m}, \quad \tau_{mm} = (2\mu + \lambda)\frac{\partial u}{\partial m} \tag{3}$$

The set of PDEs encompasses four primitive variables u, ρ, p, and e, which require the introduction of an additional equation to ensure closure of the equation system. This is done by the ideal gas equation relating pressure, temperature, and density

$$\frac{p}{\rho} = RT \tag{4}$$

The model further treats air as a calorically imperfect gas, where specific heat constant at constant pressure $c_p = f(T)$ varies with temperature. While this is less important for pressure exchangers, where temperatures can be close to ambient conditions, it becomes more important at elevated temperatures exhibited in gas turbines, where the peak cycle temperature delivered from the combustor exceeds 450–500 K [49]. Thermodynamic data for specific heat constant and internal energy used throughout this study stem from GRI-MECH [50] and the thermal database provided by Virginia Tech [51]. Finally, dynamic viscosity is modeled through the well-known Sutherland relation.

Source Terms

Viscous and Inviscid Forces. The previous one-dimensional models addressed merely viscous (friction) forces and did not directly address inviscid profile forces that account for shaft power generation. Fluid viscosity determines wall friction and promotes convective heat transfer. As a result, the corresponding source term affects both the momentum and the energy equation. Friction force is defined as

$$F_{f,\mathrm{res}} = -C_f \rho \frac{2f}{D_h} |u| u \tag{5}$$

It features a friction multiplier C_f that accounts for additional momentum losses that cannot be captured with the relatively simple approach taken. As stated by Winterbone and Pearson [52], the friction factor f is a function of the Reynolds number within the channel and is given by

$$f(\mathrm{Re}) = \begin{cases} \dfrac{0.25}{\left[\log_{10}\left(\dfrac{k}{3.7D_h} + \dfrac{5.74}{\mathrm{Re}^{0.9}}\right)\right]^2} & \text{for } 5000 \geq \mathrm{Re} \geq 10^8 \\ \dfrac{64}{\mathrm{Re}_D} & \text{for } \mathrm{Re} < 5000 \end{cases} \tag{6}$$

where k denotes the surfaces roughness value, which was set to 25 μm. Using the force diagram shown in Fig. 2(*c*), one can work out the tangential component of the friction factor and write the total source term as

$$\mathbf{S}_f = \begin{pmatrix} 0 \\ s_{f,2} \\ s_{f,3} \end{pmatrix} = \begin{pmatrix} 0 \\ -C_f \rho \dfrac{2f}{D_h} |u| u \\ \rho \dfrac{2f}{D_h} |u| c_p (T_w - T) - C_f \rho \dfrac{2f}{D_h} |u| u \dfrac{u_\theta}{u} \omega r \end{pmatrix} \tag{7}$$

Torque generation in wave rotors is pulsatile in nature and is primarily generated when the channels are exposed to a high pressure inlet port. Throughout this study, tangential forces and thus power generation are computed as a result of the momentum change as the fluid travels along the cambered channel walls.

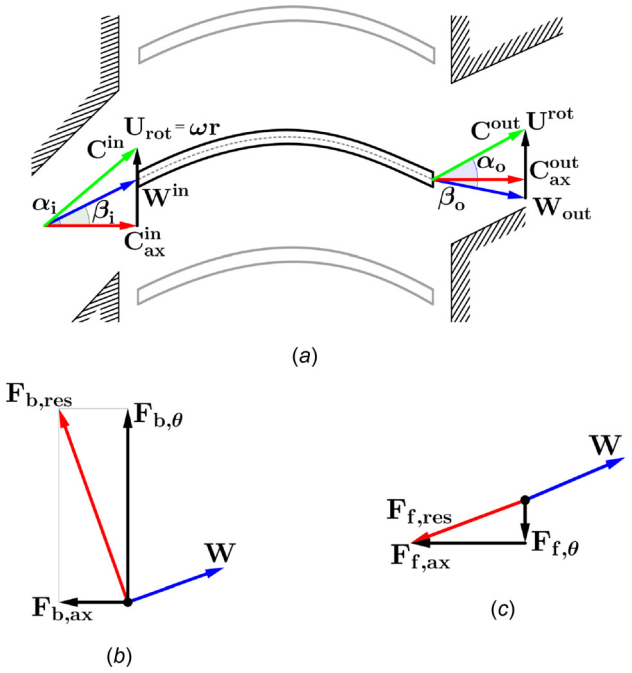

Fig. 2 (*a*) Velocity triangles at in- and outlet port over a curved rotor wall showing absolute velocity *C*, relative velocity *W*, tangential velocity *U*, and axial velocity C_{ax} with the respective absolute and relative flow angles α and β. (*b*) Inviscid blade forces and the relative flow vector. (*c*) Friction vector and the relative flow angle.

Overall, this is exemplified by the change in velocity triangles at leading and trailing edge of a passage wall, as shown in Fig. 2(*a*). The corresponding blade force source term affects momentum and energy equation and takes the form

$$\mathbf{S}_v = \begin{pmatrix} 0 \\ s_{b,2} \\ s_{b,3} \end{pmatrix} = \begin{pmatrix} 0 \\ F_{b,m} \\ F_{b,\theta} \omega r \end{pmatrix} \tag{8}$$

The tangential blade force per unit volume can be determined using the change in momentum, which is influenced by the difference in absolute tangential velocity C_θ across leading and trailing edge, the mass flow rate through the channel $\dot{m}$, and the channel volume V. In the discretized domain, this force is calculated for each element taking the difference in the tangential velocity vector from one cell to the next into account

$$F_{b,\theta} = \frac{\dot{m}}{V} (C_{\theta,o} - C_{\theta,i}) \tag{9}$$

Friction forces are accounted for by the previously suggested viscous source term. Thus, the blade force source term acts in an inviscid way so that one can assume the blade force vector to be orthogonal to the relative velocity vector, as given in Fig. 2(*b*). Hence, the scalar product of blade force vector and relative velocity vector equals zero and the equation can be rearranged to give the axial inviscid blade force per unit volume

$$\begin{aligned} \mathbf{F}_b \cdot \mathbf{U} &= 0 \\ \text{so that } F_{b,\mathrm{ax}} &= -F_{b,\theta} \frac{U_\theta}{C_{\mathrm{ax}}} \end{aligned} \tag{10}$$

In reality, the port angles will be aligned at a different angle than the passage walls angle. This can take place at off-design conditions or if an additional momentum change is desired at the stator rotor interface in order to create more torque. In addition, flow separation on the passage wall "suction side" can often be witnessed if the port angle is considerably larger than the passage wall angle. To account for such incidence losses, an additional entropy-based loss coefficient is introduced and applied in the form of a distributed loss factor. It can be calibrated through experimental data or three-dimensional CFD simulations

$$\begin{aligned} \Delta s &= -R \ln(1 - \zeta_{\mathrm{loss}}) \\ F_{\mathrm{loss},\theta} &= \frac{\rho T |C_{\mathrm{ax}}|}{|U|} \frac{\Delta s}{\Delta z} \end{aligned} \tag{11}$$

And the corresponding source term is thus

$$\mathbf{S}_{\mathrm{loss}} = \begin{pmatrix} 0 \\ s_{\mathrm{loss}_{b,2}} \\ s_{\mathrm{loss}_{b,3}} \end{pmatrix} = \begin{pmatrix} 0 \\ F_{\mathrm{loss},m} \\ F_{\mathrm{loss},\theta} \omega r \end{pmatrix} \tag{12}$$

The total tangential force and the corresponding shaft power generation are then computed as

$$\begin{aligned} F_{\theta,\mathrm{tot}} &= F_{b,\theta} - F_{f,\theta} - F_{\mathrm{loss},\theta} \\ P_{\mathrm{tot}} &= F_{\theta,\mathrm{tot}} r \omega \end{aligned} \tag{13}$$

Flow Leakage. The effect of leakage is a crucial factor in wave rotor performances and was modeled as a simple, nonlabyrinth leak in similar fashion as in the previous publications from Kentfield, NASA, and ONERA [35,39,53]. Leakage is modeled as a lumped capacitance model assuming steady flow equations. It concerns both continuity as well as energy equation, so that the leakage source term may be stated as

$$\mathbf{S}_v = \begin{pmatrix} s_{l,1} \\ 0 \\ s_{l,3} \end{pmatrix} = \begin{pmatrix} -C_D \sqrt{\frac{2\gamma}{\gamma-1}} \left(\frac{\delta_l}{h\Delta z}\right) \sqrt{p\rho}\Phi \\ 0 \\ -C_D \sqrt{\frac{2\gamma}{\gamma-1}} \left(\frac{\delta_l}{h\Delta z}\right) h\sqrt{p\rho}\Phi \end{pmatrix} \tag{14}$$

where C_D is the discharge coefficient, p and ρ the pressure and the density in channel or cavity, respectively, h denotes enthalpy, δ_l the axial clearance between rotor and stator, and Δz the cell size used for discretization. The leakage function Φ takes up the form, which allows to differentiate between flow entering and leaving the cavity depending on the pressure ratio in cell and leakage cavity

$$\begin{aligned} \Phi &= \sqrt{\left(\frac{p_{\text{cav}}}{p}\right)^{2/\gamma} - \left(\frac{p_{\text{cav}}}{p}\right)^{(\gamma+1)/\gamma}} \\ &\text{for } \frac{p_{\text{cav}}}{p} > \left(\frac{2}{\gamma+1}\right)^{\gamma/(\gamma-1)} \\ \Phi &= \sqrt{\left(\frac{2}{\gamma+1}\right)^{2/(\gamma-1)} - \left(\frac{2}{\gamma+1}\right)^{(\gamma+1)/(\gamma-1)}} \\ &\text{for } \frac{p_{\text{cav}}}{p} < \left(\frac{2}{\gamma+1}\right)^{\gamma/(\gamma-1)} \end{aligned} \tag{15}$$

The source terms are only active at the extremities of the rotor channel and are set to zero in the remainder of the domain. After each cycle, the mass and energy balance are computed, and the cavity pressure and temperature updated from a first-order system of differential equations as provided by Eq. (16). The equations designate continuity and the energy equation derived from the first law of thermodynamics and are integrated in time using an explicit Runge–Kutta scheme. Cavity pressure can be found by applying the equation of state for ideal gases

$$\begin{aligned} \frac{dm_{\text{cav}}}{dt} &= \sum_i \dot{m}_i \\ \frac{d}{dt}(m_{\text{cav}} e_{\text{cav}}) &= \dot{Q}_{\text{wht}} + \sum_i h_i \dot{m}_i \\ \text{where } e_{\text{cav}} &= c_v T_{\text{cav}} \end{aligned} \tag{16}$$

The heat transfer term stands for the heat transfer from the wave rotor wall temperature. For the respective heat transfer coefficient, a Nusselt number relation for annuli with inner cylinder rotation was used [54]

$$\text{Nu} = 0.015\left(1 + 2.3\frac{D_h}{L}\right)\left(\frac{D_o}{D_i}\right)^{0.45} \text{Re}_{\text{eff}}^{0.8}\ \text{Pr}^{1/3} = \frac{hD_h}{k} \tag{17}$$

Wall Heat Transfer. The viscous source term given in Eq. (7) features the wall temperature to compute convective heat transfer. During operation and constant inlet temperatures from the ports, the rotor temperature settles at a constant value. In order to include the effect of wall heat transfer, a lumped capacitance model that follows the first-order differential equation given in Eq. (18) was implemented

$$\begin{aligned} \frac{dT_w(t)}{dt} &= -\tau^{-1}(T_w(t) - T) \\ \text{with } \tau &= \frac{mc_p}{hA} \end{aligned} \tag{18}$$

where h is the convective heat transfer coefficient, A the surface area of heat transfer, and c_p the specific heat capacity of the solid material. The heat transfer coefficient h is determined from the Nusselt number relation for turbulent flow within a tube

$$\text{Nu} = 0.0243\ \text{Re}^{0.8}\ \text{Pr}^{0.4} = \frac{hD_h}{k} \tag{19}$$

Equation (18) is iteratively solved using a two-step Heun approach, as given in the following equation:.

$$\begin{aligned} \hat{T}_{w,i}^{n+1} &= T_{w,i}^n - \alpha\left(T_{w,i}^n - T_{g,i}^n\right)\Delta t \\ T_{w,i}^{n+1} &= T_{w,i}^n - \frac{\alpha}{2\Delta t}\left(T_{w,i}^n + \hat{T}_{w,i}^{n+1} - 2T_{g,i}^n\right) \end{aligned} \tag{20}$$

Domain Discretization. The explicit, second-order accurate scheme of Richtmyer in combination with a minmod flux limiter of Roe and Baines was selected for the discretization of the governing equations in space and time. This allows for an accurate resolution of flow discontinuities while obeying time variation diminishing criterion and preventing spurious oscillations from taking place in their vicinity. The proposed scheme suggests a two-step technique where additional half timesteps are introduced. The first step consists of a first-order accurate Lax-Friedrichs method, which can be obtained through the integration of Eq. (1) in space and time and assuming the intercell fluxes to be the average of two consecutive cells

$$\begin{aligned} \mathbf{U}_{i+1/2}^{n+1/2} &= \frac{1}{2}\left(\mathbf{U}_{i+1}^n + \mathbf{U}_i^n\right) - \frac{\Delta t}{2\Delta z}\left(\mathbf{F}_{i+1}^n - \mathbf{F}_i^n\right) - \frac{\Delta t}{4}\left(\mathbf{S}_{i+1}^n - \mathbf{S}_i^n\right), \\ \mathbf{U}_{i-1/2}^{n+1/2} &= \frac{1}{2}\left(\mathbf{U}_i^n + \mathbf{U}_{i-1}^n\right) - \frac{\Delta t}{2\Delta z}\left(\mathbf{F}_i^n - \mathbf{F}_{i-1}^n\right) - \frac{\Delta t}{4}\left(\mathbf{S}_i^n - \mathbf{S}_{i-1}^n\right) \end{aligned} \tag{21}$$

The second step uses a midpoint Leapfrog computation and consists of space and time centered differences of the mid-step solutions of $\mathbf{U}_{i\pm1/2}^{n+1/2}$ and gives

$$\mathbf{U}_i^{n+1/2} = \mathbf{U}_i^n - \frac{\Delta t}{\Delta z}\left(\mathbf{F}_{i+1/2}^{n+1/2} - \mathbf{F}_{i-1/2}^{n+1/2}\right) - \frac{\Delta t}{2}\left(\mathbf{S}_{i+1/2}^{n+1/2} - \mathbf{S}_{i-1/2}^{n+1/2}\right) \tag{22}$$

Boundary Conditions

For the implementation of boundary conditions, a cell-centered approach has been chosen. This involves the addition of an image cell lying just outside of the domain. In general, one can distinguish between inflow, outflow, and wall boundaries. For each of these types, one needs to determine the flow variables on the image cells. Walls are treated as reflective boundaries where pressure and density are equal to the neighboring interior cell node, while velocity is assigned the same value with the opposite sign.

Assuming subsonic inflow, it is necessary to specify two characteristics entering the domain, while one characteristic leaves the domain. Therefore, stagnation properties (temperature and pressure) are imposed, while velocity is extrapolated in the zeroth order. This approach further guarantees a simple way to compare results with experimental conditions. When computing the flow variables at the image cell, it is crucial to consider that the stagnation properties are defined in the absolute frame of reference, while the code operates in the relative frame of reference.

For outflows, one characteristic enters the domain, while two characteristics leave the domain. Thus, a single physical condition needs to be imposed (static outlet pressure) and the remaining two are extrapolated from the domain interior.

Unfortunately, this is only valid for fully exposed channels. There are, however, periods where only a certain portion of the channel is exposed to a port, as shown in Fig. 3(*a*). This gradual passage opening is of paramount importance in the formation of primary shock waves [55]. To account for this, a function is

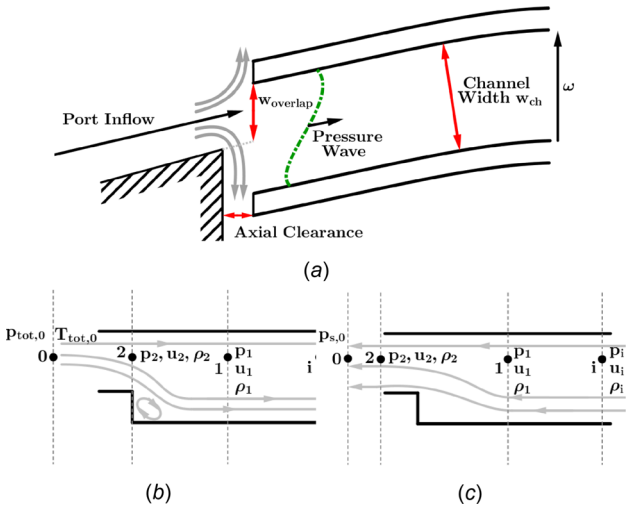

Fig. 3 (*a*) Gradual passage opening shown for port inflow. (*b*) Schematic for the boundary condition for partially open inflow. (*c*) Schematic for the boundary condition for partially open outflow.

defined that determines the amount of overlap based on port opening and closing positions, channel width, and the channel position at each time-step.

If this function is between zero and one, the port is only partially open and an alternative solution for the boundary conditions is calculated. In the case of inflow, the principle is given in Fig. 3(*b*). The gas enters the domain from a reservoir described by stagnation properties for pressure and temperature in the form of a jet through the cross section area at station 2. At station 1, the jet further expands to cover the entire width. The first cell in the domain is at station *i*. Assuming steady flow conditions, one can formulate the three conservative equations for mass, momentum, and energy between stations 1 and 2 as

$$\begin{aligned} \rho_1 u_1 A_1 &= \rho_2 u_2 A_2 \\ (p_1 + \rho_1 u_1^2) A_1 &= p_2 A_1 + \rho_2 u_2^2 A_2 \\ a_{tot} = a_1^2 + 0.5(\gamma - 1)u_1^2 &= a_2^2 + 0.5(\gamma - 1)u_2^2 \end{aligned} \tag{23}$$

giving three equations for six unknowns in total. The set of equations is closed using the energy equation and isentropic relation between stations 0 and 1 as well as wave and pathline compatibility relations [52]. In a similar fashion, one can formulate the problem for partially open outflows, as given in Fig. 3(*c*). Here, gas flowing through a cross-sectional area of A_1 exits the domain through area A_2. In the subsonic case, the pressure at station 2 equals the reservoir pressure at plane 2. Together with the conservation of mass and energy as well as the isentropic relation between stations 1 and 2 and the corresponding compatibility equations, all six unknowns can be determined.

Procedure

The solution procedure of the code shall be introduced using the example of a four-port throughflow wave rotor, as shown in the unfolded view of a single wave rotor cycle in the $z - t/\theta$ plane in Fig. 4. The ports are designated as high pressure gas inlet (HPG), high pressure air (HPA), low pressure air (LPA), and low pressure gas (LPG), referring to high pressure gas and air and low pressure air and gas, respectively.

It follows the steps outlined in Fig. 5(*b*). Initially, geometric dimensions of the rotor and target rotational speed of the wave rotor are specified. Furthermore, the number of cycles per rotation and the port solution needs to be provided. An initial guess and rough layout can be devised through the analytical tools given by

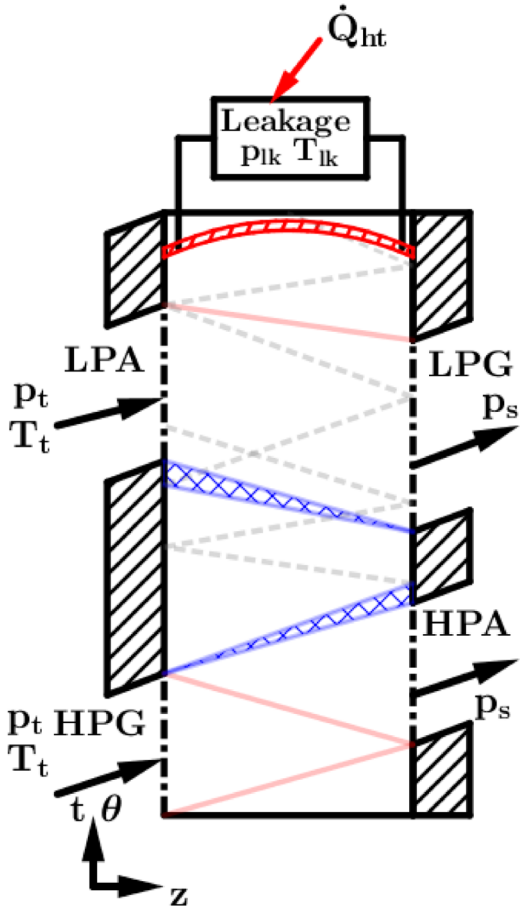

Fig. 4 Model schematic showing port arrangement and expected wave pattern for the Bath μ-wave rotor turbine. To comply with the experimental arrangement, the model was run in open loop without the inclusion of a combustor model.

Chan and Liu [43] and Müller and coworkers [56–58]. Subsequently, all matrices used throughout the computation are, along with the spatial domain, initialized. In terms of the time-step, an initial estimation is provided. While a uniform grid is used, the time-step size is allowed to vary depending on the maximum wave speed $\max_i\left(|u_i^n| + a_i^n\right)$ in the domain at the previous time-step and a fixed CFL number of 0.7 [52]. This allows us to save computational time as otherwise a constant time-step would need to suit the largest velocities in the domain and would thus have to be more on the conservative side.

In open loop configuration (without a closed combustor loop), stagnation properties in the HPG port are fixed, while static pressure in the HPA port is varied automatically using a simple proportional controller based on a simple Bernoulli relation until the mass flow rates are matched and within a 2% relative error. The low pressure inlet conditions generally involve ambient temperature of around 300 K, while the total inlet pressure again being varied in the same manner as for the HPA port and according to the desired loop flow ratio $\lambda = \dot{m}_{HPG}/\dot{m}_{LPA}$

$$p^{t+1} = p^t + \alpha \frac{\rho\left(\dot{m}_{actual}^2 - \dot{m}_{target}^2\right)}{2(\rho A)^2} \tag{24}$$

In the low pressure gas port, exhaust gases are expelled to the ambient and the static pressure is again automatically adjusted to give the desired inlet mass flow rate $\dot{m}_{HPG}$. At the end of each cycle, combustor and leakage cavity properties are updated and port flow conditions need to be determined. This is done through

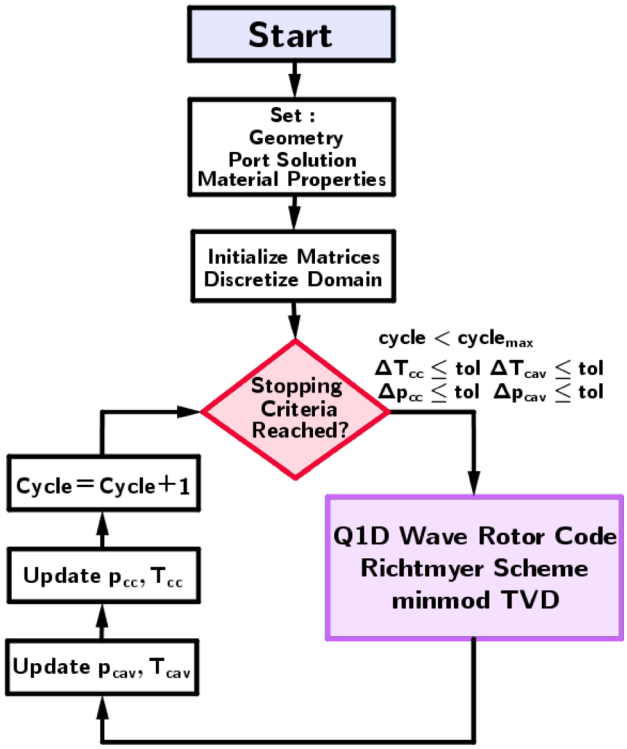

Fig. 5 Simulation model flowchart

mass flux averaging according to Eq. (25) and converting the values into the absolute frame of reference

$$\bar{\phi} = \frac{\sum_{i=N_o}^{N_c} (\phi_i \rho_i u_i)}{\sum_{i=N_o}^{N_c} (\rho_i u_i)} \tag{25}$$

Before the next cycle commences, conditions within the channel at the cycle end are set as initial conditions for the subsequent cycle, thus guaranteeing periodicity. Finally, the simulation is stopped either when the maximum number of cycles is reached or the relative changes of combustor and leakage temperature and pressures are below a predefined threshold.

Results and Discussion. The results presented in the section Results and Discussion seek to exhibit the code's ability to predict results from wave rotor experiments. This shall be done in two stages. First of all, performance data of two three-port pressure dividers are produced and compared with data from the open literature. These are Kentfield's pressure divider from the 1960s [47] and NASA pressure divider from the mid-1990 s [48]. After that, laboratory experiments conducted at the University of Bath on a μ-wave rotor turbine are used to test the code when dealing with four port, throughflow wave rotor turbines with symmetrically cambered profiles.

Table 1 Dimensions and operating conditions of Kentfield and NASA pressure divider used for the simulation

Parameter	Kentfield	NASA 3-Port
Rotor diameter (mm)	164.8	294.6
Number of channels	30	120
Channel shape	Straight	
Channel length (mm)	279.4	457.2
Channel width (mm)	15.2	6.4
Channel height (mm)	55.9	10.16
Nominal clearance (mm)	0.18	0.51
Number of cycles per revolution	3	1
Rotational speed (rpm)	6000	4150
T_{tM} (K)	308.3 K	353.9
p_{tM} (kPa)	110–150	207
p_{sL} (kPa)	100	51

Wave Rotor Pressure Dividers. The geometric dimensions and operating conditions of the two investigated designs are given in Table 1. The main characteristics of both designs shall be briefly introduced. Kentfield's device is characterized by relatively large channel width, while NASA's three-port design has four times the number of channels and has, as a consequence, a rather small channel width. Thus, it can be expected that finite opening timing effects are of minor importance. In terms of length, the NASA design is longer, so that viscous losses become more pronounced. Leakage plays a reduced role in Kentfield's experiments owing to tighter clearances between the rotor and stator endwalls.

Rotational speed of both designs and total inlet temperature in the medium pressure port are fixed in both simulations. Total inlet pressure in the medium pressure port is variable for the Kentfield experiments. In the model, the total outlet pressure of the high pressure port is varied in both cases to give a desired mass flow ratio $\dot{m}_M/\dot{m}_H$ ranging from 0.1 to 0.6. The NASA experiment was conducted at a constant mass flow ratio of 0.37. The unfolded midplane view for the two pressure exchangers with the anticipated wave pattern and relative positions of the three respective ports is given in Fig. 6. Solid red curves denote shock waves, hatched blue areas expansion fans, and dashed gray lines (weak) pressure waves.

Using the MATLAB code on Kentfield's three-port pressure divider yields the results depicted in Fig. 7. All data were produced with a grid resolution of $\Delta z/L = 0.0135$ and a discharge coefficient of 0.67 and a friction multiplier of 1.77. The plots show total pressure for the high pressure port on the ordinate and total pressure for the low pressure port on the abscissa for four different mass flow ratios. All values are nondimensionalized with respect to the inlet total pressure and inlet mass flow rate, respectively. Figure 7(*a*) shows a comparison of the 1D-Navier–Stokes equation (that includes particle friction and heat conduction in the fluid but without wall heat transfer, friction, and leakage model) compared with the experimental data. Clearly, the pressure level in the high pressure port is overpredicted with an increasing deviation toward lower pressure levels in the low pressure port. The

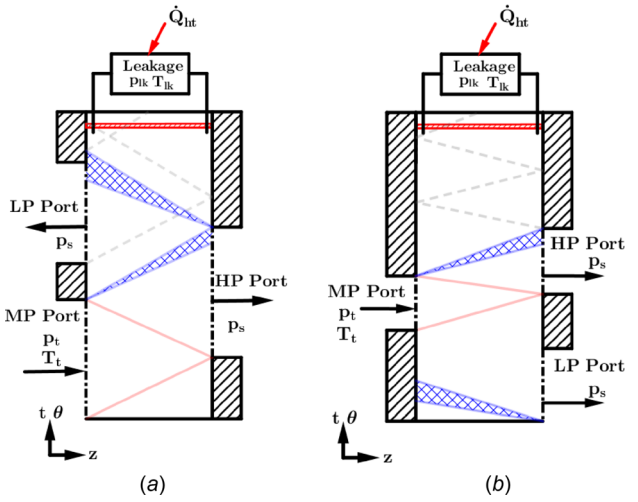

Fig. 6 Model schematic showing port arrangement and expected wave pattern for pressure dividers of (*a*) Kentfield and (*b*) NASA's Glenn Research Center

full model results are then shown in Fig. 7(*b*) outlining the effect losses impart. The main loss mechanisms responsible for the difference are leakage and friction, confirming the findings of the previous studies [35,39]. Since maximum temperatures in both cases are relatively low, wall heat transfer plays a minor role.

The same model parameters were then applied to perform unsteady validation using the NASA three-port wave rotor. This experiment featured static pressure traces at three locations, namely at $z/L = 0.025$, $z/L = 0.5$, and $z/L = 0.975$, within a wave rotor passage as it travels through the circumference. Evaluating the numerical results and normalized static pressure at the channel ends, namely at data against the numerical results, gives the distribution shown in Fig. 8. In comparison with Fig. 6(*b*), one can witness the initial expansion fan generated upon opening the low pressure port on the right-hand side. This is well captured in the model, although the expansion ratio at $z/L = 0.025$ remains slightly overpredicted. The subsequent shock discontinuity is sharper than in the experiments and features a sharp peak for both primary and secondary shock waves. The overall shock pressure ratio across all stations is, however, well depicted. The final expansion fan as well as the attenuation of the pressure wave takes place slightly sooner, as seen at around $\theta = 3.25$–3.5 rad in $z/L = 0.025$ and $z/L = 0.5$.

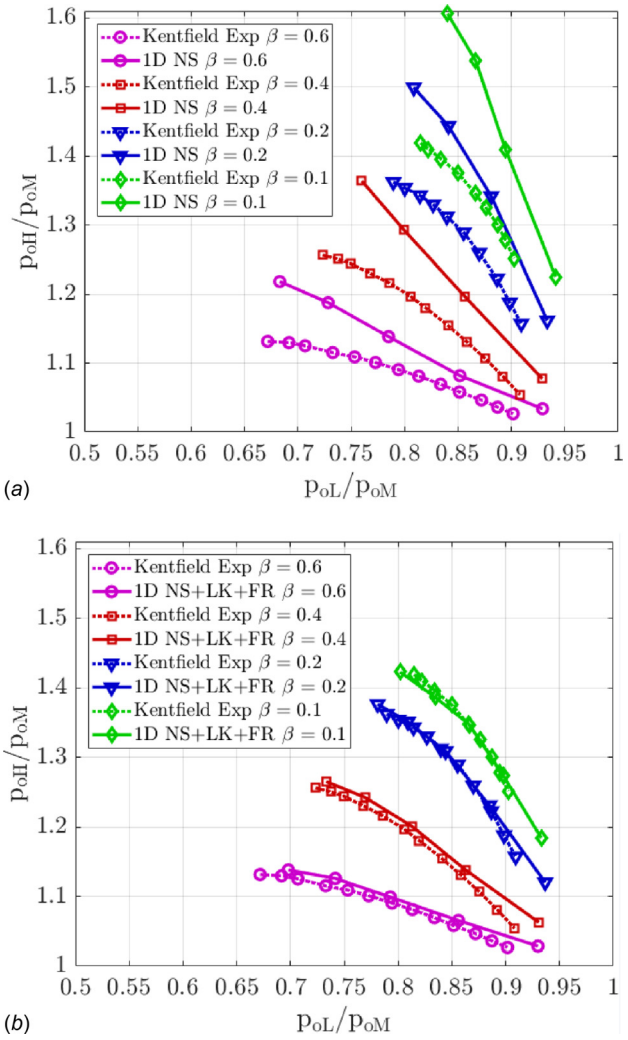

Fig. 7 Comparison of Kentfield's three-port wave rotor with the 1D simulation data. Plot shows normalized total pressure at the high pressure port versus the total pressure at the low pressure port for different mass flow ratios. (*a*) Illustrates simulation data for Euler equations without source terms, while (*b*) shows the effect of accounting for wall heat transfer, wall friction, and leakage.

Bath μ-Wave Rotor Turbine

Layout and Operating Conditions. The third validation case deals with a four-port, three-cycle throughflow wave rotor with symmetrically cambered wall profiles. The rotor was designed to yield approximately 500 W of shaft power output at a target peak cycle temperature of 750 °C and HPG total inlet pressure of 285 kPa. The port solution is shown in Fig. 4 and can be divided into a high pressure and low pressure section in the bottom and top, respectively. The former encompasses a HPG and a HPA outlet that would form the combustor loop in a gas turbine arrangement, while the latter houses the LPA inlet and a LPG outlet . A detailed view of the symmetrically cambered wall profiles and a photograph of the rotor and endplates with the corresponding port openings are given in Figs. 9(*a*) and 9(*b*).

Geometric dimensions and operating conditions that will be used for the simulations are given in Table 2. The rotor has a midwidth diameter of 60 mm, length of 30 mm, and features 46 symmetrically cambered channels with a maximum profile angle of 21.5 deg. In total, three cycles are covered in a single rotation and the design speed is set to 32,000 rpm, giving a tangential speed in the midwidth plane of 100 m/s.

The wave rotor test rig encompasses an open loop configuration, as shown in Fig. 10(*a*). A set of industrial compressors provides pressurized and dry air to the inlet side (HPG and LPA). The corresponding flow rates and thus the flow ratio λ are controlled through a set of pneumatically actuated gate valves and measured through differential mass flow meters. On the HPG leg, the incoming air is additionally directed through an air-to-air heat exchanger to use hot exhaust gases from the outlet side before being run through a set of 44 kW-electrical heaters that ensure the target inlet temperature is reached. Rotational speed and shaft power output is measured through an eddy-current dynamometer that modulates the load on the wave rotor. It is coupled to the wave rotor through a single-plane coupling. On the outlet side, further gate valves ensure the mass flow rates in the high pressure zone, i.e., between HPG and HPA, can be matched accurately before being expelled from the test chamber through extraction fans. Figure 10(*b*) exhibits a photograph from the test chamber displaying the electrical heaters as well as the wave rotor and dynamometer units and outlet gate valves.

The design of the wave rotor encompassed a variable nominal axial clearance between 0.1 and 0.4 mm. Unfortunately, it was found during the experiments that the nominal clearance differed significantly from its design value due to uneven thermal expansion. As the exact values of the actual clearances could not be determined, it was decided to use the nominal values for throughout the validation study.

Rotor Characteristics. Before moving on to the results, it is necessary to classify the wave rotor performance with respect to other existing machines. Table 3 lists a comparison of nondimensional performance parameters for finite passage opening T, viscosity F, and leakage flow G for various wave rotor types, as defined by Nagashima et al. [6] and Wilson and Fronek [48]. Although comparison is somewhat difficult for pure pressure exchangers and wave rotor turbines operating at high temperatures, one can see that the Bath μ-wave rotor performs similarly with respect to finite opening timing effects despite its short rotor length. As expected, due to the small size compared with larger designs, viscous losses become more pronounced and is similar to the microwave rotor study conducted at the University of Tokyo & ONERA [6]. The most critical loss mechanism for the investigated design is without a doubt leakage effects, which is at best similar to the ABB Comprex and the University of Tokyo. In reality, however, it is anticipated that uneven thermal expansion of stators and the shaft-rotor assembly account for a considerably

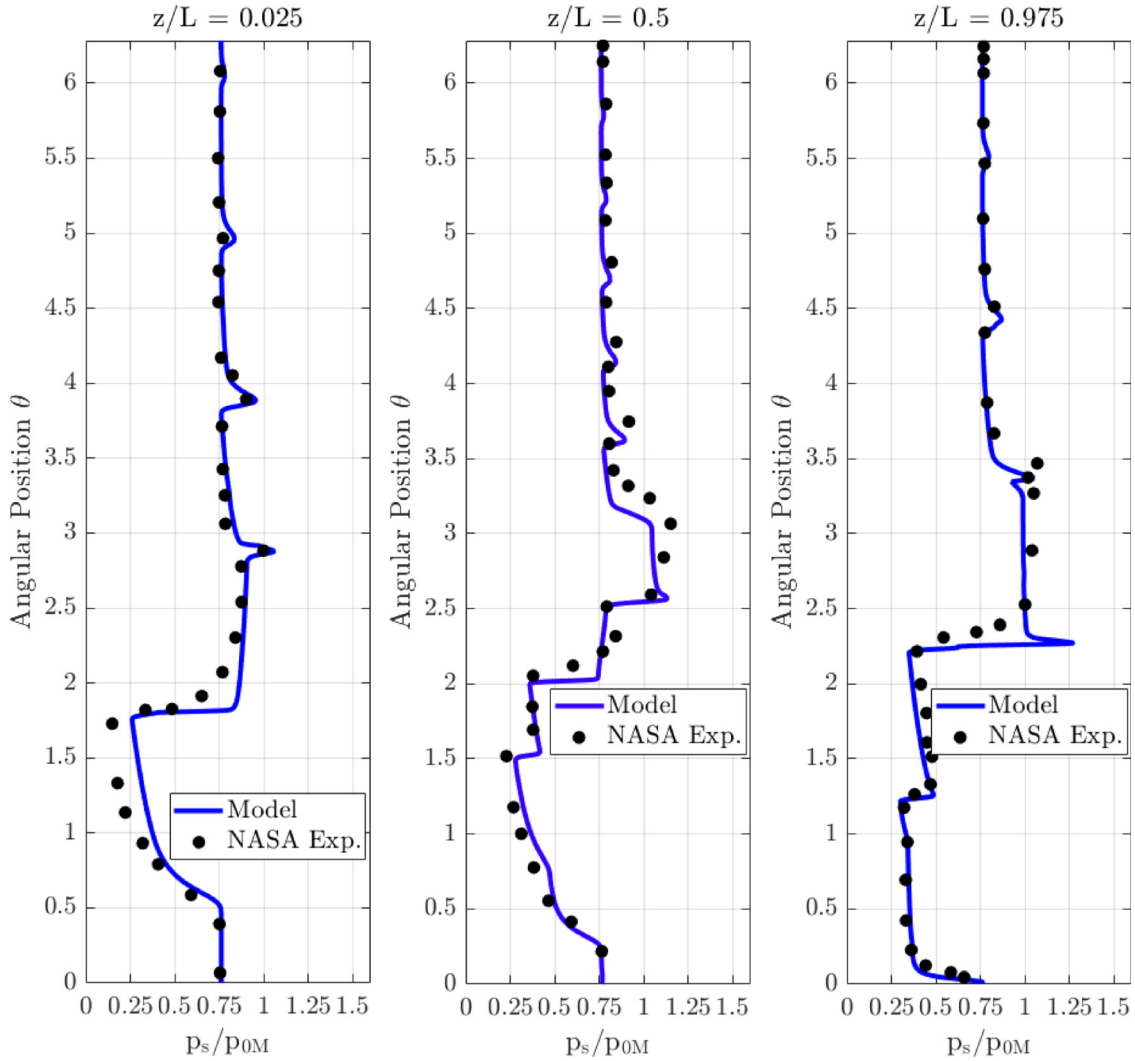

Fig. 8 Comparison of one-dimensional simulation data with experiments of a NASA three-port pressure divider at *z/L* = 0.025, *z/L* = 0.5, and *z/L* = 0.975

larger G-parameter approaching 0.2–0.23. This effect however, cannot be captured in a one-dimensional environment and needs to be taken into account through the leakage coefficient C_D. An additional effect of leakage that cannot be identified using one-dimensional code is that increasing leakage gaps promote the interaction between neighboring channels effectively attenuating in particular the reflected secondary shock extensively.

Model Validation. For the first part of the experimental validation, rotational speed was swept from 24,000 rpm to the design speed of 32,000 rpm in steps of around 2000 rpm. This is done for two different nominal leakage gaps, namely 0.20 mm on the inlet and 0.25 mm on the outlet side as well as 0.3 mm on both in- and outlet side, respectively. In addition, the peak cycle temperature $T_{t,\mathrm{HPG}}$ was varied from 500 °C to 600 °C. The loop flow ratio λ is maintained constant at 1.7. In the second part of the validation study, λ is varied in steps of 0.5 between 1.7 and 2.7. The total inlet pressure remains at approximately 270 kPa throughout.

Variations in rotational speed lead to different velocity triangles at both in- and outlet. To account for these variations and associated misalignment of the flow with the rotor profiles, a parameter fit was made for the loss coefficient ζ_{loss}. The linear relationship determined from this is given in Fig. 11(*a*) and used throughout the validation study. The same procedure was applied to the leakage coefficient C_D. Here, the situation becomes more complicated, as different leakage gaps account for slightly different characteristics, as illustrated in Fig. 11(*b*). The reason for this lies most likely in the fact that actual leakage gaps are not known and merely the nominal values were taken. Hence, the selected discharge coefficient partially accounts for this lack in information. The reason why one sees a variation of the leakage coefficient with speed can be explained by additional blockage or greater dynamic head created in the leakage gap through higher rotational speeds, similar as witnessed in turbomachinery [59]. Finally, the friction multiplier was set to 2.7 throughout the simulations. A similarly high value was witnessed in the studies by Paxson and Wilson [39].

At the design speed of 32,000 rpm Fig. 12 gives the numerically determined unfolded view of both wave pattern in the left-hand side contour plot and temperature distribution in the right-hand contour plot. The plot also shows the predicted velocity profiles in each port and the extent of gradual passage opening. Marked in stations S1 and S2 are primary (right running) and secondary shock (left running) waves generated upon opening of the high pressure gas (HPG) inlet and high pressure air (HPA) outlet. Further shown are expansion fans E1 and E2 produced as a result of HPG closing and LPG opening. The temperature distribution indicates inherent exhaust gas recirculation (EGR) characteristic to axial throughflow machines as well as a small amount of fresh air exhaustion (FAE) through the exhaust port LPG.

The effect of gradual passage opening is shown in Fig. 12(*b*), where mark T1 indicates the initiation of the primary shock wave

(*a*) (*b*)

Fig. 9 (*a*) Wave rotor turbine with and without outer sleeve showing channel curvature and (*b*) machined inlet stator exhibiting discrete port openings

before progressively increases toward the fully developed level at approximately T2. The predicted instantaneous and cycle-averaged power output for a single channel is given in Fig. 12(*c*). It becomes apparent that solely the flow entering through the HPG port results in torque generation, while opening of the LPG port and inflow through LPA does not significantly contribute to overall power generation. This is of course expected as the flow through the HPG port signifies the flow with the highest enthalpy. The total expected power output is then evaluated by multiplying the number of channels with the cycle-averaged value. The plot further indicates that the proposed symmetric, arc shape is not an optimum with respect to torque generation, which is outlined by positive regions in the instantaneous power trace near opening and closure of the HPG port.

Comparing power output, pressure ratio, and outlet temperature from the HPA duct for the experimentally determined dataset with the simulation model shows the group of plots displayed in Fig. 13. The first plot on the top left denotes total pressure ratio data obtained for a maximum inlet temperature of 500 °C and a nominal clearance of 0.20 mm on the inlet and 0.25 mm on the outlet side. The model accurately predicts the total pressure distribution well across the entire speed sweep. As expected, increased leakage gaps result in compromised energy transfer and thus lower achieved pressure ratio. This trend is reflected in the model results, although there is an overprediction in pressure ratio with a relative error between experiments and simulation of around 10–15%. Furthermore, the model predicts a pronounced drop-off in pressure ratio as one approaches lower rotational speeds, which has not been witnessed in the experiments. Opposed to the validation on pure pressure exchangers of Kentfield and NASA, there is a more pronounced discrepancy between simulation results and experimental data. This can at least partly be attributed to the fact that experimental work on pressure exchangers was done at nearly ambient temperature conditions. This renders thermal expansion effects; minimal and axial clearances between stator and rotors are likely to remain unchanged from their nominal values. For the wave rotor turbine under investigation here, peak temperatures differ significantly from ambient conditions and uneven thermal expansion between rotor and stators that cause the axial clearance gap to increase in size, which severely affects in particular the secondary shock wave strength and thus the achieved pressure ratio.

Raising maximum inlet temperature from 500 °C to 600 °C results in an increase in pressure ratio as a consequence of more enthalpy being directed to the wave rotor. While the overall trend is also reflected in the simulation results, the model indicates that the increase in temperature appears to outweigh the penalty in larger leakage flow, while in the experiments this is clearly not the case. This shortcoming exemplifies the sensitivity of the system that arises when choosing model factors, thus limiting its predictive capabilities.

Table 2 Dimensions and operating conditions of the Bath μ-wave rotor

Parameter	Bath μ-wave rotor
Rotor diameter (mm)	60
Number of channels	46
Channel shape	Sym. cambered max. $\lvert\beta_{ch}\rvert = 21.5$deg
Channel length (mm)	30
Channel width (mm)	2.9
Channel height (mm)	6
Nominal clearance (mm)	Variable 0.1–0.4
Number of cycles per revolution	3
Design rotational speed (rpm)	32,000
T_{HPG} (K)	773–883 K
p_{HPG} (kPa)	270–290
p_{LPG} (kPa)	99

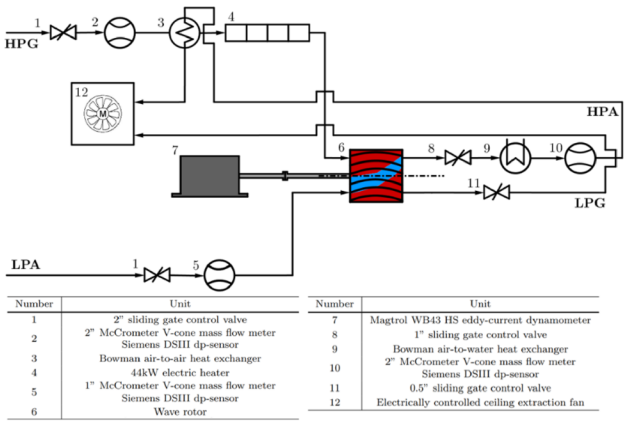

Number	Unit
1	2" sliding gate control valve
2	2" McCrometer V-cone mass flow meter Siemens DSIII dp-sensor
3	Bowman air-to-air heat exchanger
4	44kW electric heater
5	1" McCrometer V-cone mass flow meter Siemens DSIII dp-sensor
6	Wave rotor

Number	Unit
7	Magtrol WB43 HS eddy-current dynamometer
8	1" sliding gate control valve
9	Bowman air-to-water heat exchanger
10	2" McCrometer V-cone mass flow meter Siemens DSIII dp-sensor
11	0.5" sliding gate control valve
12	Electrically controlled ceiling extraction fan

(*a*)

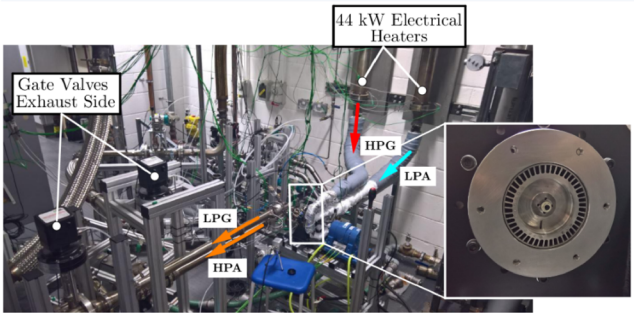

(*b*)

Fig. 10 (*a*) Schematic showing wave rotor open loop experimental setup and corresponding instrumentation. (*b*) Photograph taken from the test rig exhibiting the wave rotor, eddy-current dynamometer, electrical heaters, and outlet side gate valves.

The model yields good results with respect to predicted power output for all simulated conditions, shown in Fig. 13(*b*). Power is slightly overpredicted throughout with a relative error of around 5–10%. The power output increase shown in (b) stems from an increase in HPG mass flow rate of 34 g/s compared to 32 g/s in the low leakage case.

Finally, Fig. 13(*c*) gives a comparison of the averaged total temperature at the HPA outlet with the experimental data recorded through thermocouples close to the port outlet. Across all tested conditions, the relative error varies between 1% and 6%. While there seems to be moderate (left and right) to no (center) variation with respect to rotational speed changes, the model predicts steeper line gradients. This is a consequence of the model predictions regarding exhaust gas recirculation at the HPA port. The temperature distribution shown in Fig. 12 implies some FAE. Reducing FAE by allowing more fresh air being directed to the HPA port before the port closes. This reduces EGR rates at the HPA port and accounts for a slightly lower mixed-out temperature. This effect is well shown in Fig. 13(*a*). The simulation results in (center) and (right) almost show the same gradient with respect to speed as in the low leakage case in (left). The discrepancy between the two stems again from the effects of leakage, where increased leakage promotes interaction and flow between one channel, another channel, and the leakage cavities around it. Thus more hot air is ingested into the cold air stream leading to more or less the same average outlet temperature.

Figure 14 exhibits the effect of a variation in loop flow ratio from 1.7–2.2 and 2.7 with rotational speed. The model correctly predicts an increase in pressure ratio with increasing loop flow ratio. However, while there is a relatively small difference at a loop flow ratio of 1.7 of less than 3%, the model reacts more sensitively to an increase in loop flow ratio resulting in higher pressure ratios and increased error. Higher loop flow ratio signifies a reduced cold air mass being ingested into the wave rotor resulting in a higher average rotor temperature and thus altered thermal expansion. The Q1D-model cannot account for this change in leakage characteristic, which results in a greater error between the simulation results and the experimentally determined data.

Predicted shaft power output captures the trends of increasing power output with increasing loop flow ratio. The main mechanism for this is an increase in inlet mass flow rates to around 34 g/s at $\lambda = 2.2$ and 35.5 g/s at $\lambda = 2.7$. However, the increase indicated in the experiments is higher than shown for the simulation model, resulting at a maximum underprediction in shaft power at $\lambda = 2.7$ of approximately 8%.

Looking at the averaged temperature in the HPA port, the maximum relative error between experiments and simulations is at around 4%. The model is able to predict the effects of the decrease in fresh air flow well. Higher loop flow ratios increase EGR and thus mark a reduced effect of fresh air temperature on the mixed out average temperature. As a result, average temperatures increase as is both witnessed in the model and experiments. Furthermore, varying rotational speed has most influence on HPA outlet temperature at low loop flow ratios, where EGR rate is generally lower. At higher flow ratios, EGR rate is high and the HPA temperature less sensitive to a variation in rotational speed. This effect is recorded in the simulation results through a reduced gradient.

Conclusions and Outlook. This paper presented a numerical model that extends the previous one-dimensional codes to allow computation of torque generation in curved rotor passages through additional source terms that compute inviscid blade forces. The model was furthermore validated through both literature data and experimental data from a symmetrically cambered microwave rotor developed at the University of Bath. The main points of the paper can be summarized as follows:

- The objective of the study was to perform model validation through literature data for straight channeled pressure exchangers run at low temperature and through experimental data obtained from a symmetrically cambered microwave rotor developed at the University of Bath.
- The comparison with literature data for pressure exchangers at constant speed and inlet conditions yields good agreement for both steady and unsteady flow data. This gives confidence

Table 3 Comparison of previous wave rotors, both actually realized ones that were tested and conceptual ones (University of Tokyo/ONERA) with the Bath μ-wave rotor turbine (adapted from Ref. [6])

	Kentfield three-port PE	NASA three-port PE	NASA & R.R. Allison four-port TF	Univ. of Tokyo & ONERA micro wave rotor study	ABB Comprex four-port RF	Pearson six-port TF wave engine	Univ. of Bath four-port TF μ-wave turbine
T	0.39	0.082	0.19	0.31	0.467	0.3	0.37 at 32,000 rpm
F	0.0046	0.017	0.0037	0.012	0.0067	n.a.	0.013
G	0.0064	0.025–0.075	0.0090	0.067	0.030	n.a.	0.033–0.132

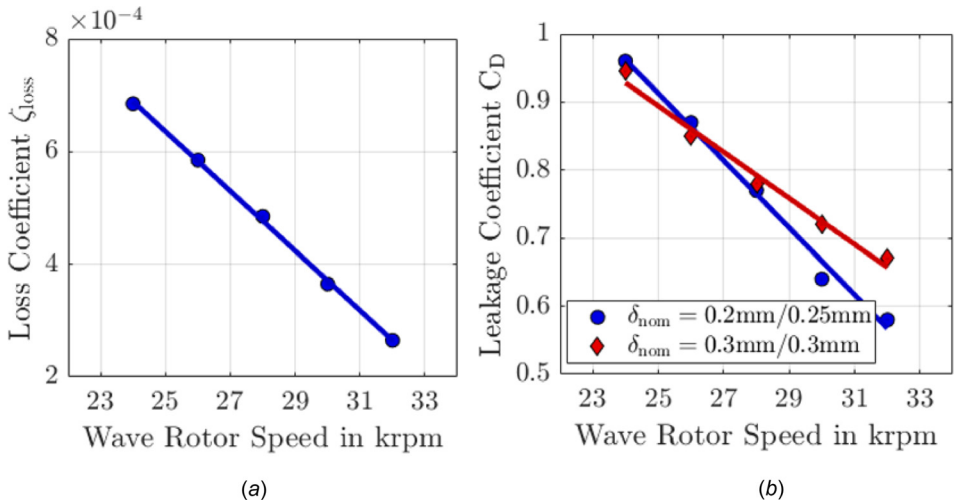

(*a*) (*b*)

Fig. 11 Parameter fit for (*a*) loss coefficient due to channel/flow misalignment and (*b*) flow leakage

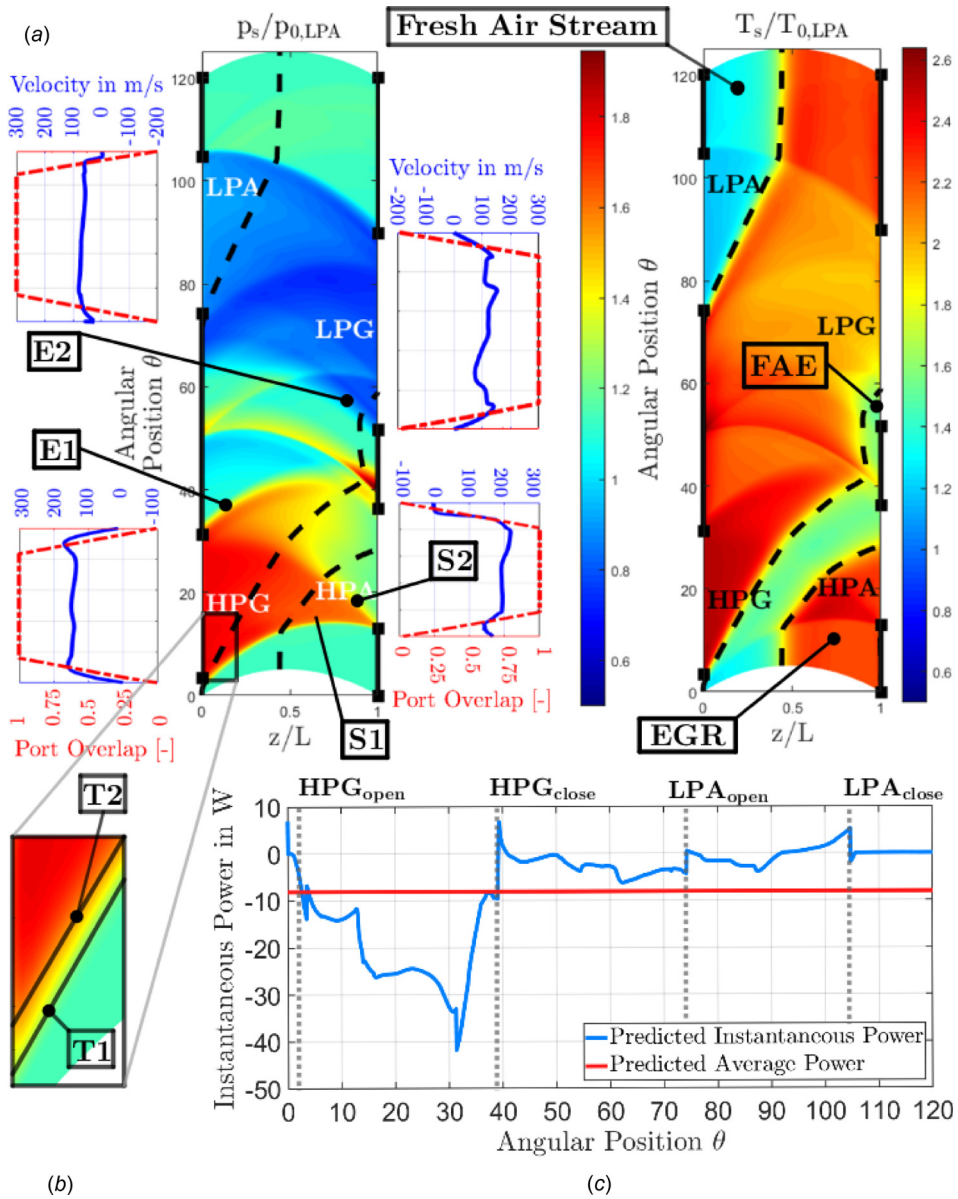

(*b*) (*c*)

Fig. 12 Q1D numerical results showing shock wave pattern, temperature field, port velocity distribution, and torque output at $\lambda = 1.7$, $N = 32{,}000$ rpm, $T_{t,\mathrm{HPG}} = 500\,^{\circ}\mathrm{C}$, and $\dot{m}_{\mathrm{HPG}} = 0.032$ kg/s

that the model is able to predict fundamental characteristics, such as wave patterns and port flow conditions. It further emphasizes the importance of loss mechanisms on the performance characteristics of wave rotors.

- A comparison of the model with sub-1 kW microwave rotor turbine data yielded promising results and showed that the model is able to identify the variation of pressure ratio and temperature with rotational speed. Predicted power output was also in very good agreement with the experimental data.

Nonetheless, a few restrictions in the model persist and can be listed as follows:

- The model appears to react more sensitively to changes in inlet temperature and leakage gap than witnessed in the experiments.
- Increases in nominal leakage lead to a larger relative error between the determined total pressure ratio for experiments and simulation. The issue is exacerbated if only the nominal, rather than the actual leakage gap for a thermally stable operating point is known rendering the determination of leakage coefficients difficult and results more deviating from experimentally determined ones.
- Power predictions are slightly overpredicted throughout, but show similar trends as in the experiments and vary only marginally with respect to changes in rotational speed. However, an additional loss factor is required to account for the (mis-)alignment of the flow at the port/rotor interface. For higher loop flow ratios, the increase in power output in the simulation results is lower

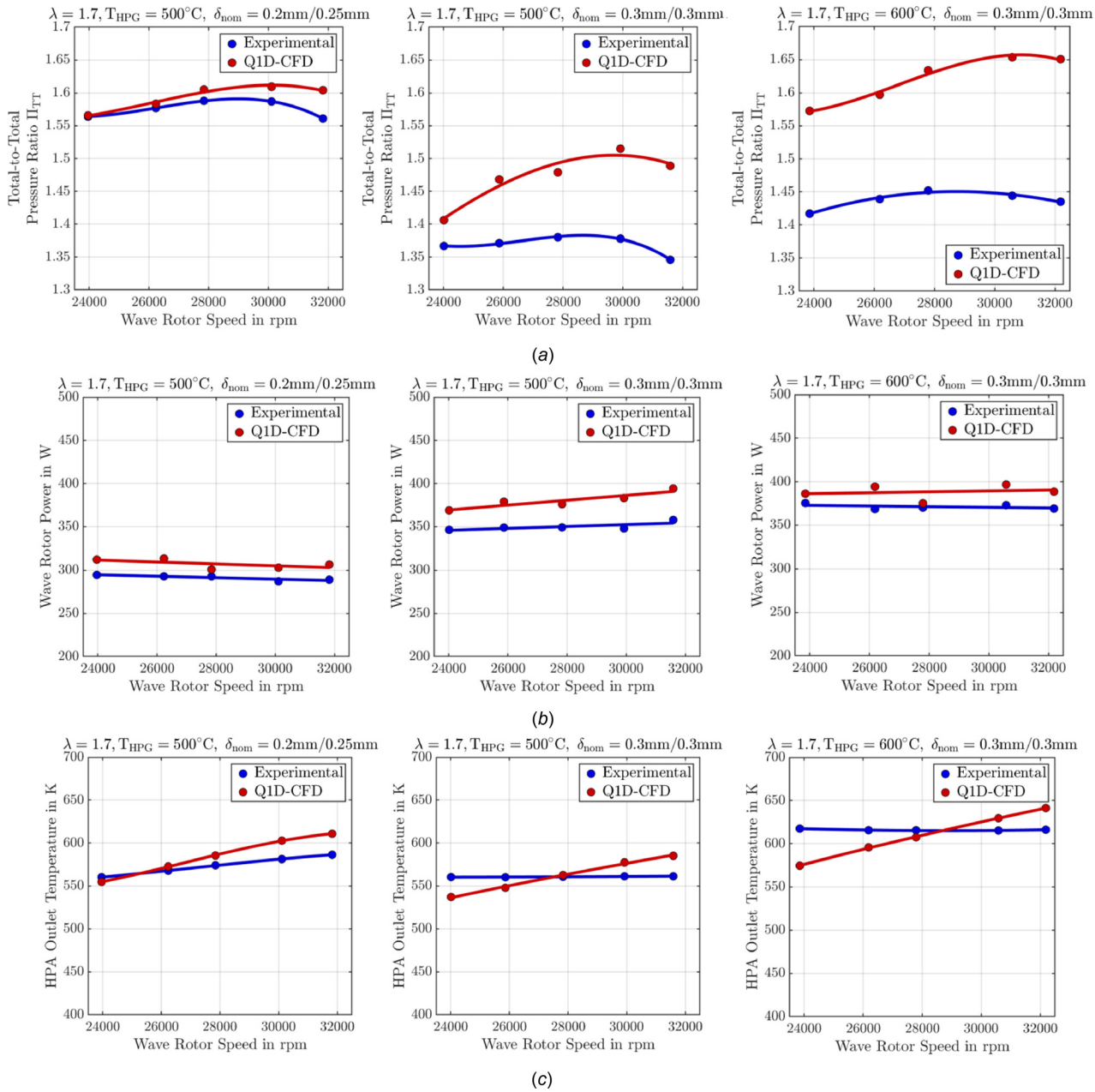

Fig. 13 Effect of leakage and peak cycle temperature variation on wave rotor performance. Comparison of experimental data and numerical model for (*a*) total-to-total pressure, (*b*) shaft power output, and (*c*) average outlet temperature in the HPA port. The graphs on the left denote data for a loop flow ratio $\lambda = 1.7$, a peak cycle temperature of 500 °C, and a nominal clearance gap of 0.2 mm on the in- and 0.25 mm on the outlet side, while graphs in the center show the effect of increased axial gap clearance to 0.3 mm and graphs on the right outline the effect of an increase in peak cycle temperature to 600 °C.

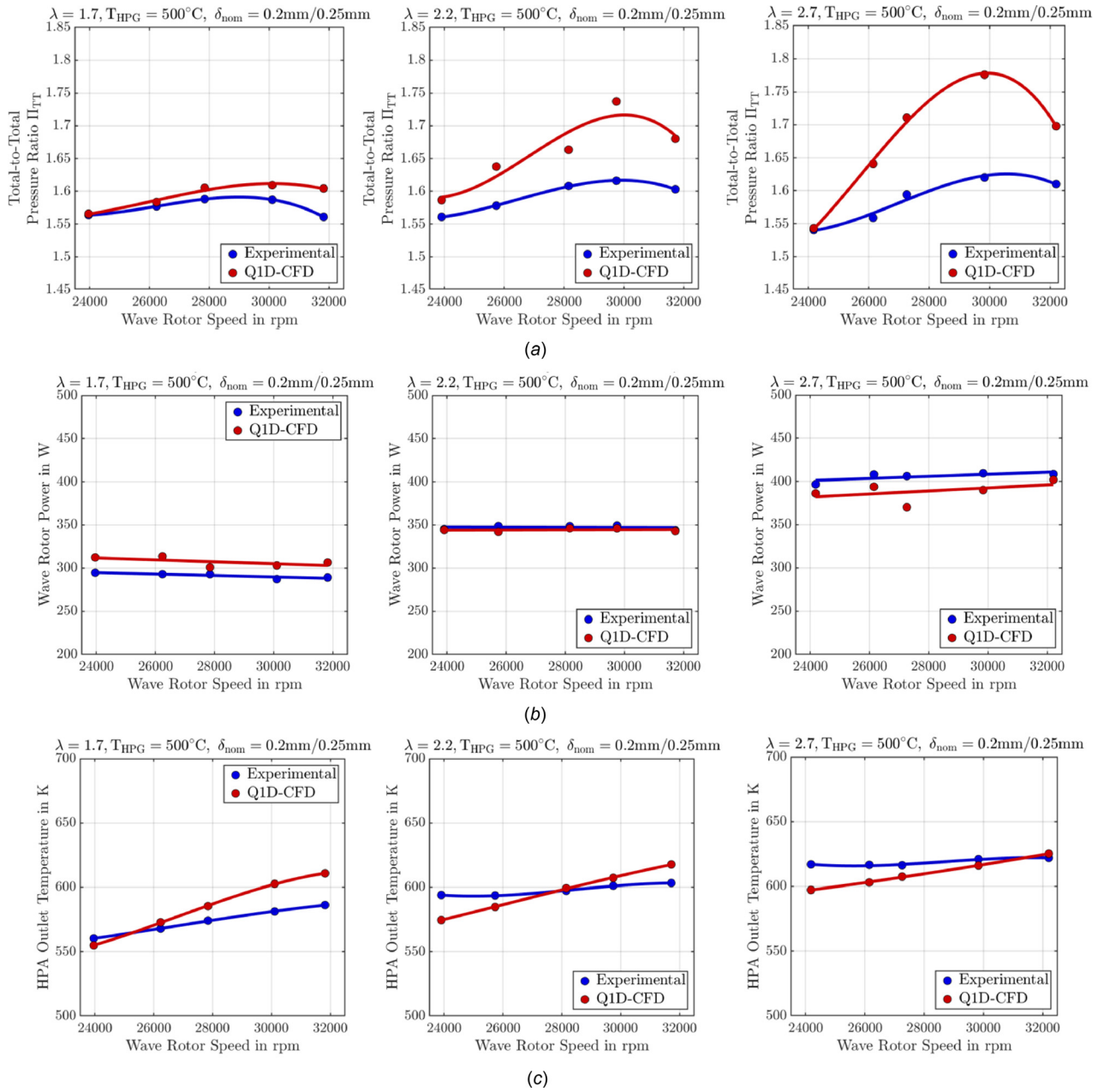

Fig. 14 Effect of loop flow ratio variation. Comparison of experimental data and numerical model for (*a*) total-to-total pressure, (*b*) shaft power output, and (*c*) average outlet temperature in the HPA port. The graphs on the left denote data for a loop flow ratio $\lambda = 1.7$, while the center plots show the results for $\lambda = 2.2$ and right-hand side graphs for $\lambda = 2.7$.

compared to the experiments, resulting in a slight underprediction for $\lambda = 2.2$.

The model is able to predict port outlet temperatures well, but fails to identify the effects larger leakage gaps incur. The effect of reduced EGR rates and thus more fresh air being directed through the HPA port appears to be more pronounced than witnessed in the experiments. Also, the ingestion of air from neighboring channels and the leakage cavity seem to become more pronounced at elevated leakage gaps, which cannot be identified by the model. However, trends showing the effect of increased loop flow ratio on the outlet temperature are captured well.

- The introduced model facilitates wave rotor turbine design process, as it provides the means to investigate both the pressure exchange capabilities of the wave rotor as well as its use as a power turbine. It can thus be used for initial sizing and as an inexpensive design tool to vary channel camber before more expensive CFD modeling tools are applied.

Acknowledgment

The authors would like to thank the Defence Science and Technology Laboratory (DSTL) for funding the project under the Defence and Security Accelerator *Beyond Battery Power* competition.

Nomenclature

a = speed of sound, m/s
A = cross-sectional area, m^2
C = absolute velocity, m/s

c_p = specific heat constant at constant pressure, J/kg K
c_v = specific heat constant at constant volume, J/kg K
C_D = leakage coefficient
C_f = friction multiplier
CFD = computational fluid dynamics
D = diameter, m
e = internal energy, J/kg
E = total energy per unit volume, J/m^3
EGR = exhaust gas recirculation
f = friction factor
F = flux vector, force per unit volume, N/m^3, nondimensional viscosity parameter
FAE = fresh air exhaustion
G = nondimensional leakage parameter in m
h = heat transfer coefficient, W/m^2 K, specific enthalpy, J/kg, channel height, m
HPA = high pressure gas
HPG = high pressure gas
k = surface roughness value, m, thermal conductivity, W/m K
LPA = low pressure air
LPG = low pressure gas
m = meridional coordinate
$\dot{m}$ = mass flow rate, kg/s
Nu = Nusselt number
p = pressure, Pa
Pr = Prandtl number
q = heat flux, W/m^2
Q = heat generation rate, W
r = radius, m
Re = Reynolds number
s = source term, specific entropy, J/kg K
t = time, s
T = temperature, K, nondimensional gradual passage opening parameter
u = velocity, m/s
U = state vector, tangential velocity, m/s
V = volume, m^3
W = relative velocity, m/s
x = spatial coordinate
α = absolute flow angle, rad, under-relaxation factor
β = relative flow angle, rad
γ = ratio of specific heats
δ = axial leakage gap, m
δz = cell size, m
ζ = loss coefficient
θ = azimuthal angle, rad
Θ = leakage function
λ = loop flow ratio
μ = dynamic viscosity, kg/m s
ρ = density, kg/m^3
τ = shear stress, N/m^2, time constant, s
ω = angular velocity, m/s

References

[1] Wilson, J., and Paxson, D. E., 1993, "Jet Engine Performance Enhancement Through Use of a Wave-Rotor Topping Cycle," NASA Memorandum No. 4486.
[2] E., Zauner, Y.-P., Chyou, F. W., and Althaus, R., 1993, "Gas Turbine Topping Stage Based on Energy Exchangers: Process and Performance," ASME Paper No. 93-GT-058.
[3] Snyder, P. H., and Fish, R. E., 1996, "Assessment of a Wave Rotor Topped Demonstrator Gas Turbine Engine Concepts," ASME Paper No. 96-GT-041.
[4] Welch, G. E., 1997, "Wave Engine Topping Cycle Assessment," AIAA Paper No. AIAA-97-0707.
[5] Welch, G. E., Jones, S. M., and Paxson, D. E., 1997, "Wave-Rotor-Enhanced Gas Turbine Engines," ASME J. Eng. Gas Turbines Power, **119**(2), pp. 469–477.
[6] Nagashima, T., Okamoto, K., and Ribaud, Y., 2005, "Cycles and Thermal System Integration Issues of Ultra-Micro Gas Turbines," RTO, Neuilly-sur-Seine, France, Educational Notes RTO-EN-AVT-131.
[7] Akbari, P., Nalim, R., and Müller, N., 2006, "Performance Enhancement of Microturbine Engines Topped With Wave Rotors," ASME J. Eng. Gas Turbines Power, **128**(1), pp. 190–202.
[8] Lenoble, G., and Ogaji, S., 2010, "Performance Analysis and Optimization of a Gas Turbine Cycle Integrated With an Internal Combustion Wave Rotor," Proc. Inst. Mech. Eng., Part A, **224**(7), pp. 889–900.
[9] Guzzella, L., Wenger, U., and Martin, R., 2000, "IC-Engine Downsizing and Pressure-Wave Supercharing for Fuel Economy," SAE Paper No. 2000-01-1019.
[10] Oguri, Y., Suzuki, T., Yoshida, M., and Cho, M., 2001, "Research on Adaption of Pressure Wave Supercharger (PWS) to Gasoline Engine," SAE Paper No. 2004-01-0368.
[11] Weber, F., Guzzella, L., and Onder, C., 2002, "Modelling of a Pressure Wave Supercharger Including External Exhaust Gas Recirculation," Proc. Inst. Mech. Eng., Part D, **216**(3), pp. 217–235.
[12] Suzuki, T., Oguri, Y., K, U., and Yoshida, M., 2004, "Experimental Investigation of Pressure Wave Supercharging for SI Engine," ASME Paper No. IMECE2004-62419.
[13] Spring, P., Onder, C. H., and Guzzella, L., 2007, "EGR Control of Pressure-Wave Supercharger IC Engines," Control Eng. Pract., **15**(12), pp. 1520–1532.
[14] Yan, L., Dasen, Z., Hongguang, Z., Changwei, J., Jiangguo, L., and Tong, Z., 2008, "Experiment and CFD Investigation of Pressure-Wave Supercharger," SAE Paper No. 2008-01-1631.
[15] Pohořelský, L., Macek, J., Polášek, M., and Vítek, O., 2004, "Simulation of a COMPREX Pressure Exchanger in a 1-D Code," SAE Paper No. 2004-01-1000.
[16] Lei, Y., Zhou, D. S., and Zhang, H. G., 2010, "Investigation on Performance of a Compression-Ignition Engine With Pressure-Wave Supercharger," Energy, **35**(1), pp. 85–93.
[17] Zhao, J., and Hu, D., 2017, "An Improved Wave Rotor Refrigerator Using an Outside Gas Flow for Recycling the Expansion Work," Shock Waves, **27**(2), pp. 325–332.
[18] Hu, D., Li, R., Liu, P., and Zhao, J., 2016, "The Loss in Charge Process and Effects on Performance of Wave Rotor Refrigerator," Int. J. Heat Mass Transfer, **100**, pp. 497–507.
[19] Hu, D., Li, R., Liu, P., and Zhao, J., 2016, "The Design and Influence of Port Arrangement on an Improved Wave Rotor Refrigerator Performance," Appl. Therm. Eng., **107**, pp. 207–217.
[20] Pekkan, K., and Nalim, M. R., 2003, "Two-Dimensional Flow and NO_x Emissions in Deflagrative Internal Combustion Wave Rotor Configurations," ASME J. Eng. Gas Turbines Power, **125**(3), pp. 720–730.
[21] Nalim, M. R., Izzy, Z. A., and Akbari, P., 2012, "Rotary Wave-Ejector Enhanced Pulse Detonation Engine," Shock Waves, **22**(1), pp. 23–38.
[22] M. Rajagopal, A. K., and Nalim, R., 2012, "Wave-Rotor Pressure-Gain Combustion Analysis for Power Generation and Gas Turbine Applications," ASME Paper No. GTINDIA2012-9741.
[23] Pearson, R. D., 1985, "A Gas Wave-Turbine Engine Which Developed 35 HP and Performed Over a 6:1 Speed Ranges," ONR/NAVAIR Wave Rotor Research and Technology Workshop.
[24] Pearson, R. D., 1986, "Thermodynamics and Gas Dynamics of Internal Combustion Engines, Volume II," *The Oxford Handbook of Innovation*, D. E. Winterbone, and S. C. Low, ed., Oxford University Press, Oxford, UK.
[25] Mathur, A., 1985, "Design and Experimental Verification of Wave Rotor Cycles," ONR/NAVAIR Wave Rotor Research and Technology Workshop.
[26] R., Taussig, P., Cassady, J. Z. W. T., and Klostermannt, E., 1983, "Investigation of Wave Rotor Turbofans for Cruise Missile Engines," Final Report Submitted by MSNW to DARPA (Contract N00140-82-C-9729).
[27] Weber, H. E., 1996, *Shock Wave Engine Design*, Wiley, New York.
[28] Mathur, A., and Shreeve, R. P., 1987, "Calculation of Unsteady Flow Processes in Wave Rotors," AIAA Paper No. 87–0011.
[29] Mathur, A., 1986, "Code Development for TurbofanEngine Cycle Performance With and Without a Wave Rotor Component," Naval Postgraduate School, Monterey, CA, Report No. NPS67-86-006CR.
[30] Roberts, J. W., 1990, "Further Calculations of the Performance of Turbofan Engines Incorporating a Wave Rotor," M.S. thesis, Naval Postgraduate School, Monterey, CA.
[31] Salacka, T. F., 1985, "Review, Implementation and Test of the QAZID Computational Method With a View to Wave Rotor Applications," M.S. thesis, Naval Postgraduate School, Monterey, CA.
[32] Johnston, D. T., 1987, "Further Development of a One-Dimensional Unsteady Euler Code for Wave Rotor Applications," M.S. thesis, Naval Postgraduate School, Monterey, CA.
[33] Okamoto, K., and Nagashima, T., 2003, "A Simple Numerical Approach of Micro Wave Rotor Gasdynamic Design," 16th International Symposium on Airbreathing Engines, Cleveland, OH, Aug. 31–Sept. 5, Paper No. ISABE-2003-1213.
[34] Okamoto, K., Nagashima, T., and Yamaguchi, K., 2003, "Introductory Investigation of Micro Wave Rotor," International Gas Turbine Congress 2003, Tokyo, Japan.
[35] Fatsis, A., Lafond, A., and Ribaud, Y., 1998, "Preliminary Analysis of the Flow Inside a Three-Port Wave Rotor by Means of a Numerical Models," Aerosp. Sci. Technol., **2**(5), pp. 289–300.
[36] Fatsis, A., Orfanoudakis, N. G., Pavlou, D. G., Panoutsopoulou, A., and Vlachakis, N., 2006, "Unsteady Flow Modelling of a Pressure Wave Supercharger," Proc. Inst. Mech. Eng. Part D, **220**(2), pp. 209–218.
[37] Iancu, F., Piechna, J., and Müller, N., 2005, "Numerical Solutions for Ultra-Micro Wave Rotors (UμWR)," AIAA Paper No. 2005-5034.
[38] Paxson, D. E., 1992, "A General Numerical Model for Wave Rotor Analysis," NASA Lewis Research Center, Cleveland, OH, Report No. NASA-TM-105740.
[39] Paxson, D., and Wilson, J., 1993, "An Improved Numerical Model for Wave Rotor Design and Analysis," AIAA Paper No. 93–0482.

[40] Paxson, D. E., and Wilson, J., 1995, "Recent Improvements to and Validation of the One Dimensional NASA Wave Rotor Model," NASA Lewis Research Center, Cleveland, OH, Report No. NASA-TM-106913.
[41] Paxson, D. E., 1995, "A Numerical Model for Dynamic Wave Rotor Analysis," AIAA Paper No. 95–2800.
[42] Welch, G. E., and Paxson, D. E., 1998, "Wave Turbine Analysis Tool Development," NASA Lewis Research Center, Cleveland, OH, Report No. NASA/TM–1998-208485.
[43] Chan, S., and Liu, H., 2017, "Mass-Based Design and Optimization of Wave Rotors for Gas Turbine Engine Enhancement," Shock Waves, **27**(2), pp. 313–324.
[44] Chan, S., Liu, H., Xing, F., and Song, H., 2018, "Wave Rotor Design Method With Three Steps Including Experimental Validation," ASME J. Eng. Gas Turbines Power, **140**(11), p. 111201.
[45] Mustafa, A., Martinez-Botas, R. F., Pesiridis, A., Chiong, M. S., and Rajoo, S., 2014, "Assessment of Turbocharger Turbine Unsteady Flow Modelling Methodology on Engine Performance," ASME Paper No. ESDA2014-20392.
[46] Costall, A., 2007, "A One-Dimensional Study of Unsteady Wave Propagation in Turbocharger Turbine," Ph.D. thesis, Imperial College London, London.
[47] Kentfield, J. A. C., 1969, "The Performance of Pressure-Exchanger Dividers and Equalizers," ASME J. Basic Eng., **91**(3), pp. 361–369.
[48] Wilson, J., and Fronek, D., 1993, "Initial Results From the NASA-Lewis Wave Rotor Experiment," AIAA Paper No. 93–2521.
[49] Witte, D. W., Tatum, K., and Williams, S. B., 1996, "Computation of Thermally Perfect Compressible Flow Properties," AIAA Paper No. 96-0681.
[50] Smith, G. P., Golden, D. M., Frenklach, M., Moriarty, N. W., Eiteneer, B., Goldenberg, M., Bowman, C. T., Hanson, R. K., Song, S., Gardiner, W. C., Jr., Lissianski, V. V., and Qin, Z., 2019, "GRI-Mech 3.0," The Gas Research Institute, accessed July 30, 2019, http://www.me.berkeley.edu/grimech/
[51] Martin, C. R., 2010, "HOT: Thermodynamic Tools for Matlab," Virginia Active Combustion Control Group, accessed July 29, 2019, http://hot-tdb.sourceforge.net/
[52] Winterbone, D. E., and Pearson, R. J., 2000, *Theory of Engine Manifold Design: Wave Action Methods for IC Engines*, Professional Engineering Publishing Limited, London.
[53] Kentfield, J. A. C., 1993, *Nonsteady, One-Dimensional, Internal, Compressible Flows*, Oxford Engineering Sciences, Oxford, UK.
[54] Kuzay, T. M., and Scott, C. J., 1977, "Turbulent Heat Transfer Studies in Annulus With Inner Cylinder Rotation," ASME J. Heat Transfer, **99**(1), pp. 12–19.
[55] Larosiliere, L. M., 1993, "Three-Dimensional Numerical Simulation of Gradual Opening in a Wave Rotor Passage," AIAA Paper No. 93–2526.
[56] Akbari, P., and Müller, N., 2003, "Preliminary Design Procedure for Gas Turbine Topping Reverse-Flow Wave Rotors," International Gas Turbine Congress, Tokyo, Japan.
[57] Akbari, P., and Müller, N., 2003, "Gas Dynamic Design Analyses of Charging Zone for Reverse-Flow Pressure Wave Superchargers," ASME Paper No. ICES2003-0690.
[58] Iancu, F., Piechna, J., and Müller, N., 2008, "Basic Design Scheme for Wave Rotors," Shock Waves, **18**(5), pp. 365–378.
[59] Denton, J. D., 1993, "Loss Mechanisms in Turbomachines," ASME J. Turbomach., **115**(4), pp. 621–656.